Nonreciprocity and zero reflection in nonlinear cavities with tailored loss

S. R. K. Rodriguez,[1,*] V. Goblot,[2] N. Carlon Zambon,[2] A. Amo,[3] and J. Bloch[2]

[1]*Center for Nanophotonics, AMOLF, Science Park 104, 1098 XG Amsterdam, The Netherlands*

[2]*Centre de Nanosciences et de Nanotechnologies, CNRS, Université Paris-Sud, Universit Paris-Saclay, 91120 Palaiseau, France*

[3]*Université Lille, CNRS, UMR 8523–PhLAM–Physique des Lasers Atomes et Molécules, F-59000 Lille, France*

We demonstrate how to tailor the losses of nonlinear cavities in order to suppress their reflection and enhance their nonreciprocal transmission. We derive analytical expressions predicting the existence of zero-reflection channels in single and coupled nonlinear cavities, depending on the driving frequency and loss rates. While suppressing the reflection from a single cavity imposes a stringent condition on the input-output leakage rates, we demonstrate that this condition can be significantly relaxed in systems of coupled cavities. In particular, zero-reflection and nonreciprocity can be achieved across a range of driving frequencies in coupled cavities by tuning the output leakage rate alone. Numerical calculations based on the driven-dissipative Gross-Pitaevskii equation, usually employed to describe microcavity polaritons, reveal the spatial phenomenology associated with zero-reflection states and provide design guidelines for the construction of nonlinear optical isolators.

Lorentz reciprocity, which in the absence of gain and loss is equivalent to time-reversal symmetry [1], states that the relationship between source and detector remains unchanged when their positions are exchanged. Reciprocity holds for linear time-invariant systems with symmetric permittivity and permeability tensors [2]. Systems not constrained by Lorentz reciprocity are of interest in many fields, particularly in photonics since they may function as optical diodes or isolators [3–21]. Figure 1 illustrates two main features of an ideal optical isolator: light propagates one way only, and reflection at the input port is zero.

Recently, many efforts have concentrated on the design of compact magnetic-free nonreciprocal systems. One approach to nonreciprocity is based on dynamic modulation—a departure from the time-invariance assumption on which Lorentz reciprocity relies [5,9,13,22–25]. An alternative approach to nonreciprocity is based on the combination of nonlinearity and spatial symmetry breaking [3,6,11,12,18,19,21,26]. While every approach to nonreciprocity offers benefits and limitations [27,28], a common drawback of many approaches is that reflection from the input port tends to be deleteriously high at nonreciprocal conditions; see, for example, Table 1 of Ref. [7], comparing insertion losses and nonreciprocity for several systems.

Here we take a different approach to simultaneously achieve nonreciprocity and zero reflection from the input port of dissipative cavities with Kerr-type nonlinearity. Our approach relies on tailoring the leakage rates of the cavities to their input-output ports. In contrast to previous approaches combining Fano and Lorentzian resonances with a suitable delay line in-between [21], our method works for coupled cavities even when their eigenfrequencies and intrinsic loss rates are equal. To benchmark our results, we first provide

a detailed analysis of nonreciprocity in a single nonlinear cavity with separate input-output ports. In the presence of intrinsic cavity losses, nonreciprocity with zero reflection can only be achieved for a particular value of the input-output leakage rate difference. As we will show, this stringent condition can be relaxed in systems of coupled cavities. We find analytical expressions for the conditions giving zero reflection in nonreciprocal systems of single and coupled cavities. In addition, through numerical calculations based on the driven-dissipative Gross-Pitaevskii equation, we present a design for a realistic semiconductor polariton system where our predictions can be experimentally tested.

I. SINGLE NONLINEAR CAVITY

Figure 1(b) illustrates the system studied in this section: a single-mode cavity with resonance frequency ω_0, intrinsic loss rate γ, and a χ^3 Kerr-type nonlinearity leading to photon-photon interactions of strength U. The cavity is coupled to two separate input-output ports at rates $\kappa_{1,2}$. A monochromatic field of frequency ω and amplitude F drives the cavity through port 1. Within the mean-field approximation neglecting quantum fluctuations [29,30], the cavity field amplitude ψ obeys the following equation of motion ($\hbar = 1$):

$$i\dot{\psi} = \left(\omega_0 - i\frac{\Gamma}{2} + U|\psi|^2\right)\psi + i\sqrt{\kappa_1}Fe^{-i\omega t}, \quad (1)$$

where $\Gamma = \gamma + \kappa_1 + \kappa_2$ is the total loss. The steady-state solutions are found by setting $\dot{\psi} = 0$ and inserting the ansatz $\psi(t) = \psi e^{-i\omega t}$ in Eq. (1). For convenience, we move to a frame rotating at the driving frequency ω. In this rotating frame, the detuning $\Delta = \omega - \omega_0$ is the relevant energy parameter and $Fe^{-i\omega t} \to F$. The steady-state field is then a solution
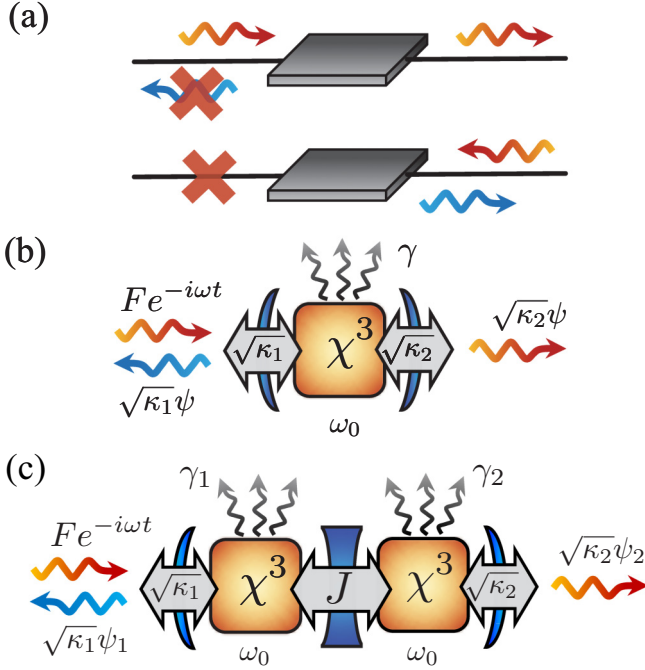
*s.rodriguez@amolf.nl

FIG. 1. (a) Ideal features of an optical isolator: zero reflection and high transmission for forward propagation (top panel), and zero transmission for backward propagation (bottom panel). (b) Sketch of a single-mode cavity with Kerr-type nonlinearity, intrinsic loss γ, and coupled to two separate input-output ports at rate $\kappa_{1,2}$. (c) Sketch of two coupled cavities [each one as in (b)] with coupling energy J. In both (b) and (c), the resonant system is driven from the left (port 1) by a monochromatic field of frequency ω and amplitude F. For testing the reciprocity of the system, the driving field is switched to the right (not shown).

to the following algebraic equation:

$$0 = \left(-\Delta - i\frac{\Gamma}{2} + U|\psi|^2 \right)\psi + i\sqrt{\kappa_1}F. \tag{2}$$

Once ψ is obtained, the transmittance $\mathcal{T}$ and reflectance $\mathcal{R}$ can be calculated as follows:

$$\mathcal{T}_1 = \left| \frac{\sqrt{\kappa_2}\psi}{F} \right|^2 = \frac{\kappa_1\kappa_2}{(\Delta - Un)^2 + \Gamma^2/4}, \tag{3}$$

$$\mathcal{R}_1 = \left| \frac{F - \sqrt{\kappa_1}\psi}{F} \right|^2 = 1 - \frac{\kappa_1(\kappa_2 + \gamma)}{(\Delta - Un)^2 + \Gamma^2/4}, \tag{4}$$

with $n = |\psi|^2$ the number of photons in the cavity. The subscript "1" of $\mathcal{R}$ and $\mathcal{T}$ indicates that the cavity is driven through port 1. Similar expressions can be obtained for $\mathcal{R}_2$ and $\mathcal{T}_2$ by letting $1 \to 2$ and $2 \to 1$, and solving Eq. (2) again for n. Notice that if $\gamma \neq 0$, $\mathcal{R} + \mathcal{T} < 1$.

While Eqs. (3) and (4) seem to be symmetric in κ_1 and κ_2, the response of the system is not the same when driven through port 1 and port 2 because of the nonlinear term Un. Indeed, for $\kappa_1 \neq \kappa_2$, driving through the ith port instead of through the jth ports rescales the effective drive amplitude by $\sqrt{\kappa_i}/\sqrt{\kappa_j}$. For a fixed F, this results in a different n when driving through ports 1 and 2. Consequently, the cavity transmission is nonreciprocal when the input ports are switched.

Notice that whereas the transmittance is simply proportional to $|\psi|^2$, the reflectance is determined by the interference between the driving field and the cavity field. In particular, $\mathcal{R}_1$ vanishes when $F = \sqrt{\kappa_1}\psi$, corresponding to total destructive interference between the two fields. Substituting this relation in Eq. (2), we find two necessary conditions for $\mathcal{R}_1 = 0$:

$$\kappa_1 = \kappa_2 + \gamma = \Gamma/2,$$
$$F_c^2 = \kappa_1\Delta/U, \tag{5}$$

with F_c the critical driving amplitude for which $\mathcal{R}_{1,c} = 0$. Hereafter, the quantities evaluated at $F = F_c$ will have the "c" subscript. If the conditions in Eq. (5) hold, the transmittance is $\mathcal{T}_{1,c} = \kappa_2/\kappa_1$. This leads to the following conclusion: unitary transmission requires $\gamma = 0$ and $\kappa_1 = \kappa_2$. The latter would imply that the device is mirror-symmetric and, therefore, it would not show any nonreciprocity. Hence, in this configuration, either unitary transmission or nonreciprocity can be achieved, but not both simultaneously.

To quantify the nonreciprocity, we need to define an appropriate figure of merit. Nonreciprocity has been previously assessed through the ratio of forward-to-backward transmission at a fixed intensity [4,7]. Alternatively, an isolation intensity range can be defined as the ratio of input intensities from opposite propagation directions that lead to the same transmission [21]. Applying these definitions to nonlinear systems exhibiting bistability or multistability is nontrivial. A bistable cavity sustains two stable steady states with different photon numbers at the same driving conditions [31]. The observed steady state depends on the driving history of the system; hysteresis emerges as a driving parameter is scanned across a bistability [32,33]. Since $\mathcal{T}$ cannot be uniquely defined within the hysteresis range, the isolation ratio is also not uniquely defined. In principle, this ambiguity can lead to asymmetric forward-to-backward transmission at fixed driving conditions if the system is biased into different states, even for symmetric systems. To avoid this ambiguity, we propose to evaluate $\mathcal{T}$ not only at equal F, but also at equal driving histories. For instance, if the cavity is driven across a hysteresis cycle in the forward direction, then the same driving protocol should be followed in the backward driving direction. For bistable cavities, this criterion gives the "worst possible" isolation ratio (I) as follows:

$$I = \frac{\mathcal{T}_{1,\max}}{\mathcal{T}_{2,\max}}. \tag{6}$$

$\mathcal{T}_{1,\max}$ and $\mathcal{T}_{2,\max}$ are the maximum transmittance one can obtain when driving the system from port 1 or 2, respectively. For $\kappa_1 = \kappa_2$, one finds using Eq. (3) that $I = 1$, i.e., the system is reciprocal. Meanwhile, for asymmetric systems ($\kappa_1 \neq \kappa_2$) with more than one possible forward-to-backward transmission ratio, our definition of I gives the value closest to 1, i.e., the worst possible isolation ratio for a given input power.

Let us now analyze the nonreciprocal behavior of a single bistable cavity with $\kappa_1 \neq \kappa_2$. For repulsive interactions $U > 0$, bistability occurs for $\Delta > \sqrt{3}\Gamma/2$. Within the hysteresis cycle range, the intracavity photon number n is constrained by $n_- \leqslant n \leqslant n_+$, with $n_\pm = (2\Delta)/(3U) \pm (6U)^{-1}\sqrt{4\Delta^2 - 3\Gamma^2}$. The black (gray) shaded areas in Fig. 2(a) enclose the values of
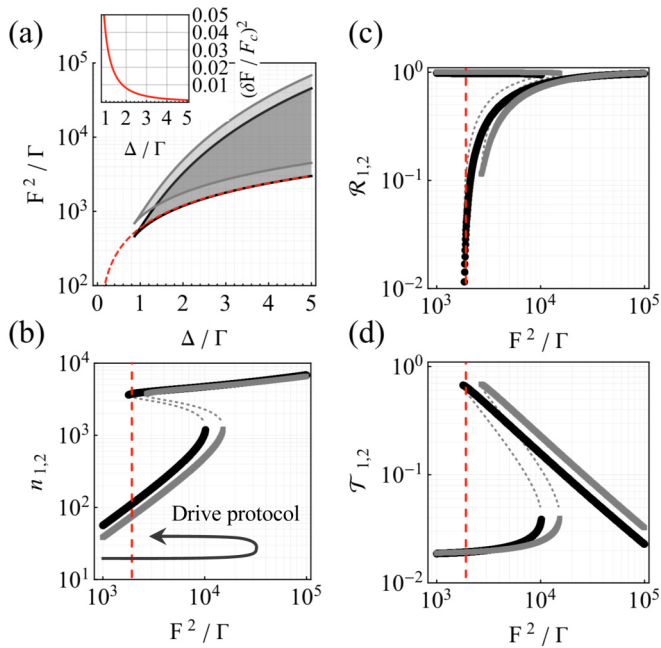
FIG. 2. Calculations for a single cavity as depicted in Fig. 1(b), with $U = 0.005\gamma$, $\kappa_1 = \Gamma/2$, $\kappa_2 = \Gamma/3$, and $\gamma = \Gamma/6$. (a) Black (gray) curves enclose the range of normalized driving power F^2/Γ and normalized laser-cavity detunings Δ/Γ, with $\Delta = \omega - \omega_0$, giving rise to bistability when driving through port 1 (port 2). The inset shows the largest power fluctuation $(\delta F/F_c)^2$ the system can withstand without losing its nonreciprocity by falling from the bistability branch with the largest number of photons; F_c is the critical driving amplitude at which $\mathcal{R}_1 = 0$. (b), (c), and (d) Number of photons in the cavity, reflectance, and transmittance, respectively, all for $\Delta/\Gamma = 3$. The vertical black line in (c) and (d) indicates the critical drive power for which the reflectance vanishes, as predicted by Eq. (5).

F^2/Γ and Δ/Γ where bistability takes place when driving through port 1 (port 2). Here and throughout the paper, the same color code will be used for quantities computed when driving through the two ports. The shape of the bistability region is the same when driving through ports 1 and 2, but this region is shifted to higher F when driving through port 2 because $\kappa_2 < \kappa_1$.

In Fig. 2(b) we plot n versus F^2/Γ for a weakly nonlinear cavity $U \ll \gamma$ at the detuning $\Delta = 3\Gamma$, where the system displays a bistable behavior. The stability of the solutions was assessed by evaluating the spectrum of small fluctuations around the steady state [29]. Unstable solutions are indicated by gray dashed lines. As we have set $\kappa_1 = \Gamma/2 = \kappa_2 + \gamma$ to satisfy Eq. (5) for the calculations in Fig. 2(b), at fixed F and for finite γ, the effective driving strength through port 1 is greater than through port 2. Consequently, the bistability range is shifted in F and the transmission is nonreciprocal.

Figures 2(c) and 2(d) show $\mathcal{R}_{1,2}$ and $\mathcal{T}_{1,2}$, respectively, corresponding to the steady-state solutions in Fig. 2(b). Notice in Fig. 2(c) the sharp dip in $\mathcal{R}_1$. To access this state, one needs to apply the drive protocol sketched in Fig. 2(b) to reach the high n state very close to the bistability falling edge (not jumping down) when driving through port 1. $\mathcal{R}_1 = 0$ at the power indicated by the dashed line in Fig. 2(c), which is the

critical drive amplitude $F_c = \kappa_1 \Delta/U$ predicted by Eq. (5). A finite $\mathcal{R}_1$ is observed in the numerical calculations because of the finite step size in F. Figure 2(d) shows that for $\mathcal{R}_1 = 0$, $\mathcal{T}_1 = 1/2$ and $\mathcal{T}_2 \ll 1$: driving through port 2 at the same F can only set the system in the low-n branch, such that $I \approx 36$. In this regime, starting from Eq. (3), we can deduce an approximate formula for the isolation ratio at F_c,

$$I_c \approx 1 + \frac{4\Delta^2}{\Gamma^2}, \tag{7}$$

where we used the fact that $\mathcal{T}_{2,c} \approx \kappa_1\kappa_2/(\Delta^2 + \Gamma^2/4)$ because the term Un is negligible in the low-n steady state. Interestingly, in the regime we are considering in which the driving field intensity is in between the two down-falling bistability edges shown in Fig. 2(b), the I does not depend on the relative values of $\kappa_{1,2}$ and γ; it only depends on the ratio of the detuning Δ to the total loss Γ.

Vanishing $\mathcal{R}_1$ and nearly unitary transmission can be achieved in the limit of arbitrarily small but finite γ as long as $\kappa_1 = \kappa_2 + \gamma$. However, this makes it increasingly difficult to unidirectionally bias the system into the desired bistable state because the difference between the left- and right-driven bistability threshold diminishes when γ vanishes. A similar argument holds for the isolation ratio. Even if I_c can be made arbitrarily high by increasing Δ/Γ, the difference δF between F_c and the value of F corresponding to the falling edge of the high n steady state becomes increasingly small. Consequently, tiny fluctuations in the input power ($\propto F^2$) have an increasing probability of making the cavity switch to the low n steady state where there is poor isolation and high reflectance. A relevant figure of merit for practical implementations is the ratio $(\delta F/F_c)^2$. This ratio quantifies the largest power fluctuation that the system can withstand without losing its nonreciprocity. We plot this quantity in the inset of Fig. 2(a) as a function of Δ/Γ. For $\Delta/\Gamma = 3$ as considered in Figs. 2(b)–2(d), power fluctuations of 0.5% will spoil both the isolation and low-reflectance of the system.

We now seek an expression for the maximum transmission $\mathcal{T}_{1,*}$ (or correspondingly, minimum reflection $\mathcal{R}_{1,*}$) which can be achieved at a certain $\kappa_{1,2}$ and γ, while driving through port 1. From Eqs. (3) and (4), we see that this is achieved for $\Delta = Un$. The drive amplitude F_* yielding $\mathcal{T}_{1,*}$, $\mathcal{R}_{1,*}$ can also be determined by plugging the latter condition in Eq. (2). We get

$$\mathcal{T}_{1,*} = \frac{4\kappa_1\kappa_2}{\Gamma^2}, \quad \mathcal{R}_{1,*} = \frac{(\gamma - \kappa_1 + \kappa_2)^2}{\Gamma^2},$$
$$F_*^2 = \frac{\Gamma^2}{4}\frac{\Delta}{\kappa_1 U}. \tag{8}$$

The isolation ratio can be obtained by computing $\mathcal{T}_2$ at the drive amplitude F_*. These results, together with Eq. (7), completely determine the best achievable performance in terms of $\mathcal{R}$, $\mathcal{T}$, and I, as well as the driving amplitude at which this condition manifests, for any set of parameters (Δ, U, $\kappa_{1,2}$, γ).

To illustrate how the performance degrades when departing from the condition $\kappa_1 = \kappa_2 + \gamma$, we compute and report in Fig. 3 $\mathcal{R}_{1,*}$, $\mathcal{T}_{1,*}$, and I as a function of κ_2 and Δ for $\gamma = 0.02$ meV and $\kappa_1 = 0.06$ meV. These are experimentally relevant parameters as explained later. The horizontal dashed
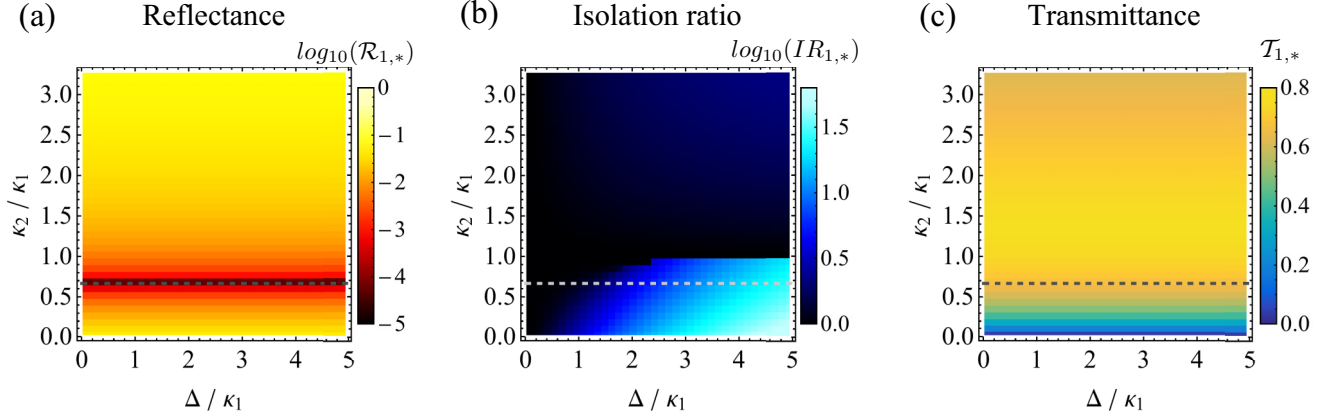
FIG. 3. Calculations for a single cavity as depicted in Fig. 1(b), with $U = 0.005\gamma$, $\gamma = \kappa_1/3$, and $\kappa_2/\kappa_1 = 2/3$. (a), (b), (c) Reflectance, isolation ratio, and transmittance in color scale as a function of the leakage rate ratio κ_2/κ_1 and normalized laser-cavity frequency detuning Δ/κ_1. The horizontal dashed line indicates the value of κ_2/κ_1 leading to zero reflection, as predicted by Eq. (5).

line in all panels indicates the value of κ_2 for which $\mathcal{R}_1 = 0$. Increasing κ_2 above this ideal value degrades the system in terms of $\mathcal{R}_{1,*}$ and I. Decreasing κ_2 below the ideal value improves I but degrades the performance both in terms of $\mathcal{R}_{1,*}$ and $\mathcal{T}_{1,*}$. In contrast, as we will see in Sec. II, tuning κ_2 in coupled cavities allows $\mathcal{R}_1 = 0$, high $\mathcal{T}_1$, and high I at variable values of Δ.

In summary, for single Kerr resonator, either unitary transmission ($\gamma = 0$) or nonreciprocity can be achieved. If we allow finite losses ($\gamma \neq 0$) and the mirror symmetry of the system is broken ($\kappa_1 \neq \kappa_2$), a nonlinear steady state with $\mathcal{R}_1 = 0$ and an isolation ratio growing quadratically with Δ/Γ [see Eq. (7)] can be achieved. However, to achieve this effect, strict conditions have to be met for the ratios of the input-output couplings $\kappa_{1,2}$ with respect to the losses γ, which may limit the performance of realistic implementations of the scheme. Such strict conditions can be relaxed in systems of two coupled resonators.

II. TWO COUPLED NONLINEAR CAVITIES

In this section, we consider two mutually coupled cavities as depicted in Fig. 1(c). Notice that ports 1 and 2 are now connected to different cavities. As we will show, this allows relaxing the stringent conditions on the loss rates leading to zero reflection at the input port while still maintaining high nonreciprocity.

In a frame rotating at the driving frequency ω, the equations for the coupled cavity fields are

$$\left(-\Delta_1 - i\frac{\Gamma_1}{2} + Un_1\right)\psi_1 - J\psi_2 = -i\sqrt{\kappa_1}F, \quad (9)$$

$$\left(-\Delta_2 - i\frac{\Gamma_2}{2} + Un_2\right)\psi_2 - J\psi_1 = 0 \quad (10)$$

with ψ_j the field, $\Delta_j = \omega - \omega_j$ the laser-cavity detuning, $\Gamma_j = \gamma + \kappa_j$ the total loss, and $n_j = |\psi_j|^2$ the number of photons in the jth cavity ($j = 1, 2$). J is the coupling between the two cavities. Calculating ψ_j (see Appendix B for details) allows us to get the steady-state photon numbers n_j and to assess the stability of the steady states [34]. For brevity, we

omit details of the stability analysis, which can be found in Ref. [34]. We only recall that the coupled equations (9) and (10) admit multiple steady states at certain driving conditions, i.e., multistability. Each state can be classified as (i) stable, (ii) single-mode unstable, or (iii) parametrically unstable [34]. Here, we are interested in finding stable steady states leading to minimum reflection at the input port and high transmission.

The transmittance $\mathcal{T}$ and reflectance $\mathcal{R}$, when driving through port 1, can be defined as follows:

$$\mathcal{T}_1 = \left|\frac{\sqrt{\kappa_2}\psi_2}{F}\right|^2, \quad (11)$$

$$\mathcal{R}_1 = \left|\frac{F - \sqrt{\kappa_1}\psi_1}{F}\right|^2. \quad (12)$$

Comparing Eqs. (11) and (12) with Eqs. (3) and (4) reveals an important feature of coupled cavities with respect to a single cavity. The cavity field responsible for $\mathcal{R}_1$, namely ψ_1, is not the field responsible for maximizing $\mathcal{T}_1$, namely ψ_2. This feature opens new possibilities to achieve $\mathcal{R}_1 = 0$ and high nonreciprocity over extended parameter ranges.

Next, we pose the following question: Given a pair of identical cavities with eigenfrequency ω_0, intrinsic loss γ, and mutual coupling J, for which values of the parameters $\Delta = \Delta_1 = \Delta_2$ and $\kappa_{1,2}$, can we observe $\mathcal{R}_1 = 0$? Our question is relevant to optical experiments, where Δ and $\kappa_{1,2}$ are typically external parameters that can be adjusted *in situ*. Δ can be adjusted with a tunable laser, while $\kappa_{1,2}$ can be adjusted in evanescently coupled cavity-waveguide systems by tuning the cavity-waveguide distance, for example.

In Appendix B we address the above question by deriving analytical expressions guaranteeing the existence of a zero-reflection state. Unlike for a single cavity, we find two solutions giving $\mathcal{R}_1 = 0$ for coupled cavities. One of these solutions is equivalent to Eq. (5) (details ahead). The additional solution guaranteeing $\mathcal{R}_1 = 0$ in the coupled cavity case reads

$$\Delta^2 = (\kappa_1 + \kappa_2)^2 \left(\frac{J^2}{(\kappa_1 - \gamma)(\kappa_2 + \gamma)} - \frac{1}{4}\right). \quad (13)$$
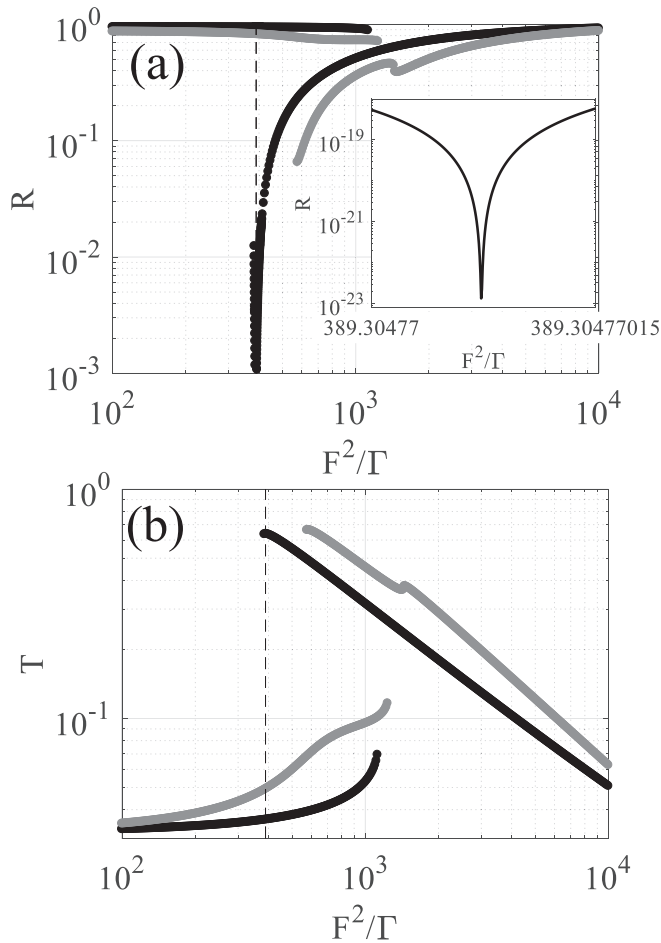
FIG. 4. Reflectance (a) and transmittance (b) calculated for two coupled cavities as depicted in Fig. 1(c), with $J = 0.1$ meV, $\gamma = 0.02$ meV, $U = 0.07$ μeV, $\kappa_1 = 0.06$ meV, and $\kappa_2 = 0.4494$ meV. Black and gray curves correspond to driving through port 1 and port 2, respectively. The dashed line in both panels indicates the critical driving power for which the reflectance vanishes. The inset of (a) is a zoom into the reflectance dip.

In the derivation of Eq. (13), we also find that $\mathcal{R}_1 = 0$ requires $n_2 \Gamma_2 = n_1 \tilde{\Gamma}_1$, with $\tilde{\Gamma}_1 = \kappa_1 - \gamma$. This result demonstrates the key role that the losses play in achieving $\mathcal{R}_1 = 0$ by controlling the power flow through the system and fixing the relative number of photons in the two cavities.

Next, we numerically solve Eqs. (9) and (10) and calculate $\mathcal{R}_1$ and $\mathcal{T}_1$ as a function of F^2/Γ. Figures 4(a) and 4(b) show $\mathcal{R}_1$ and $\mathcal{T}_1$ for values of J, U, γ, and $\kappa_{1,2}$, given in the caption. These values correspond to an experimentally realizable configuration to be discussed in the next section. The detuning was set to $\Delta = 4.513\kappa_1$ to satisfy Eq. (13) in combination with the other parameters.

Figure 4(a) displays a sharp dip in $\mathcal{R}_1$ at $F^2/\Gamma = 389.3$. The inset of Fig. 4(a) shows a zoom into the dip, evidencing that $\mathcal{R}_1$ is suppressed by $\sim$23 orders of magnitude, limited by machine precision. At the driving power for which $\mathcal{R}_1 = 0$, nonreciprocity with $I = 13$ is obtained [see Fig. 4(b)]. The small jump in $\mathcal{R}_2$ and $\mathcal{T}_2$ around $F^2/\Gamma = 1450$ in the main panel is associated with an additional bistability. Cascades of bistabilities and multistabilities emerging when driving one

of two coupled cavities have been previously studied [34] and experimentally observed [35,36].

Next, we assess $\mathcal{R}$, $\mathcal{T}$, and the isolation ratio I [Eq. (6)] for systematic variations of the coupled cavity system parameters. To this end, we first calculate $\mathcal{R}$ and $\mathcal{T}$ over a wide range of F for a system with fixed Δ, U, $\kappa_{1,2}$, γ, and J. We perform this calculation first driving through port 1 and then driving through port 2. The F-scan starts at low values for which the system is in the linear regime, and ends at high values that are well above all nonlinear thresholds. We then search for $\mathcal{R}_{1,*}$, i.e., the minimum value of $\mathcal{R}_1$, and estimate the corresponding value of the transmission $\mathcal{T}_{1,*}$. We also evaluate I at the driving amplitude F_* corresponding to $\mathcal{R}_{1,*}$. The results of similar calculations for various Δ and κ_2, keeping $\kappa_1 = 0.06$ meV and $J = 0.1$ meV constant, are presented in Fig. 5. Figures 5(a)–5(c) correspond to a system with $\gamma = \kappa_1/3$, and Figs. 5(d)–5(f) correspond to $\gamma = 0$. The dark regions in Figs. 5(a) and 5(d) indicate the parameters for which the reflectance vanishes.

Besides the numerical results, all panels of Fig. 5 display two analytical predictions for $\mathcal{R}_1 = 0$. The green dashed curve, which depends on Δ, follows from Eq. (13), with $\kappa_1 = 0.06$ meV and $J = 0.1$ meV; this frequency-dependent solution, enabling $\mathcal{R}_1 = 0$ at any κ_2, is exclusive to coupled cavities. In contrast, the gray dashed line independent of Δ in all panels of Fig. 5 corresponds to a solution in which the two cavities effectively behave as a single one. In this case, the reflectance minimum takes place at $\kappa_2 = \kappa_1 - 2\gamma$, which can be recognized as the counterpart of Eq. (5) for a single cavity if one lets $\gamma \to 2\gamma$ considering that we have twice the intrinsic losses in the effective single cavity. Overall, our analytical and numerical results demonstrate that $\mathcal{R} = 0$ can be achieved across a wide range of κ_2 by tuning Δ. This tunability is impossible to achieve with a single cavity, where $\mathcal{R} = 0$ only occurs for $\kappa_1 = \Gamma/2$ regardless of Δ.

We proceed to analyze the influence of γ on I by comparing Figs. 5(b) and 5(e). Notice in Fig. 5(e) that $I \approx 1$ (black region in the color plot) at the values of κ_2 and Δ for which $\mathcal{R}_1 = 0$ along the green dashed line. Thus, for $\gamma = 0$ there is negligible isolation when $\mathcal{R} = 0$. In contrast, high I and $\mathcal{R}_1 = 0$ can be simultaneously achieved for a broad range of κ_2 when $\gamma \neq 0$. This is evidenced by the overlap of the green dashed line and the less dark region of the color plot in Fig. 5(b). These results highlight how adding intrinsic loss γ offers the possibility to tune the parameters (κ_2, Δ) so as to achieve simultaneously suppressed reflectance and high nonreciprocity.

Simultaneously achieving high I and $\mathcal{R}_1 = 0$ by setting $\gamma \neq 0$ and tuning κ_2 requires $J > \kappa_1, \gamma$ [37]. This result follows from Eq. (13), which for $J < \kappa_1, \gamma$ leads to purely imaginary detunings Δ. Physically, $J < \kappa_1, \gamma$ means that the two cavities act as if they are being decoupled. Consequently, the $\mathcal{R}_1 = 0$ solution that is only present in coupled cavities vanishes. In contrast, for $J > \kappa_1, \gamma$ there is a finite range of κ_2 for which Δ is real; these are physically realizable $\mathcal{R}_1 = 0$ states. Further increasing J above κ_1, γ enlarges the range of κ_2 and Δ over which high I and $\mathcal{R}_1 = 0$ can be simultaneously achieved. Note that while J needs to be greater than both κ_1 and γ for coupled cavity physics to emerge, J can
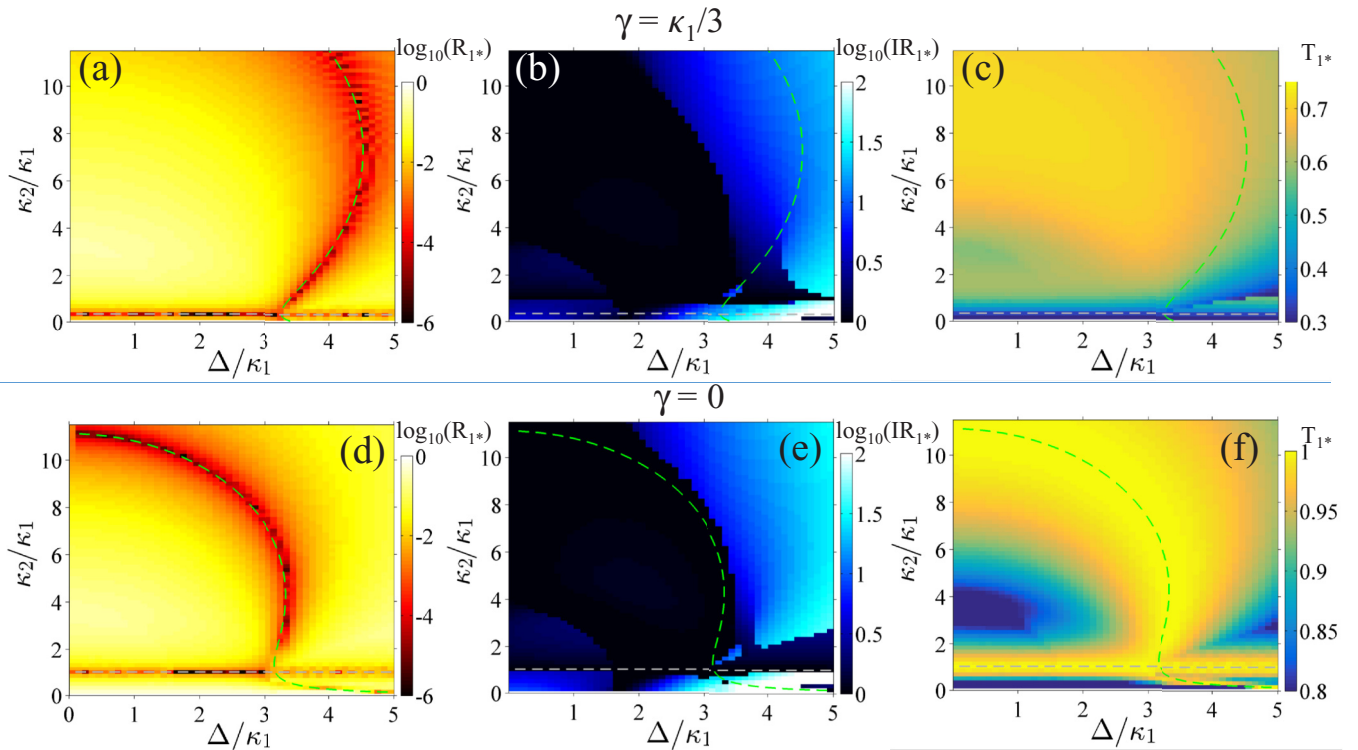
FIG. 5. Calculations for two coupled cavities as depicted in Fig. 1(c), with $J = 0.1$ meV, $U = 0.07$ μeV, and $\kappa_1 = 0.06$ meV. In panels (a), (b), and (c) $\gamma = \kappa_1/3$, and in panels (d), (e), and (f) $\gamma = 0$. Panels (a) and (d) show the minimum reflectance $\mathcal{R}_{1,*}$ observed at any driving power F^2. Panels (b) and (e) show the isolation ratio I at the same power for which $\mathcal{R}_{1,*}$ was observed. Panels (c) and (f) show the transmittance $\mathcal{T}_{1,*}$ of the same state associated with $\mathcal{R}_{1,*}$. Note that $\mathcal{R}_{1,*}$ and I are plotted in log scale, while $\mathcal{T}_{1,*}$ is plotted in linear scale. The green dashed curves in all panels are analytical predictions for zero reflection from Eq. (13); this state is exclusive to coupled cavities. The gray dashed curves in all panels are analytical predictions for zero reflection based on Eq. (5), but letting $\gamma \rightarrow 2\gamma$ because we have two dissipative cavities; this state corresponds to effective single-cavity behavior.

be much less than the total losses $2\gamma + \kappa_1 + \kappa_2$ provided that Eq. (13) is satisfied.

The ability to simultaneously achieve high I and $\mathcal{R}_1 = 0$ by setting $\gamma \neq 0$ and tuning κ_2 comes at the expense of a degraded total transmission, as Figs. 5(c) and 5(f) show. Whereas unitary transmission can be achieved for $\gamma = 0$ [Fig. 5(f)], for $\gamma = \kappa_1/3$ [Fig. 5(c)] the transmittance is limited to a maximum value around 0.75. The tradeoff between unitary transmission and nonreciprocity for two identical coupled cavities also exists for a single cavity. However, by introducing intrinsic loss γ in the coupled cavity system, high transmittance is traded for the ability to tune the parameters (κ_2, Δ) leading to $\mathcal{R}_1 = 0$. In contrast, giving away high transmittance through a single cavity by introducing intrinsic loss does not enable one to tune any of the parameters to achieve $\mathcal{R} = 0$.

In this section, we have focused on two coupled nonlinear cavities that are identical. One may wonder to what extent the physics of nonreciprocity and zero reflection is robust to deviations in the resonance frequencies of the cavities, which may result from fabrication imperfections. When these deviations are much smaller than the cavity loss rates and the intercavity coupling, the physics remains qualitatively the same. Such systems of practically identical strongly coupled highly nonlinear optical cavities have already been realized in the laboratory [36,38]. The more general case in which

$\Delta_1 \neq \Delta_2$ has the only result of changing the driving frequency where the zero reflection happens by an amount proportional to the energy difference between the bare cavity resonances. This additional degree of freedom can actually be used to further enhance nonreciprocity, as theoretically demonstrated by Sato and co-workers [39,40].

III. DRIVEN-DISSIPATIVE GROSS-PITAEVSKII CALCULATIONS

In this section we propose a design, based on polaritons in semiconductor microcavities, for the experimental implementation of nonreciprocity and zero reflection using nonlinearity in coupled resonators. Polaritons are quasiparticles arising from the strong coupling between excitons confined in a quantum well and photons in a cavity [41]. Polaritons mutually interact due to their excitonic component, giving rise to strong Kerr-type optical nonlinearities [42]. Several techniques are known for confining polaritons and for coupling confined polariton modes [36,43–48].

We consider a microstructure schematically represented in Fig. 6, which could be fabricated via deep etching of a planar microcavity. The microstructure is made of two coupled pillars linked in an asymmetric way to a one-dimensional waveguide via two constrictions. This 2D structure can be mapped to an effective 1D potential for polaritons. We make
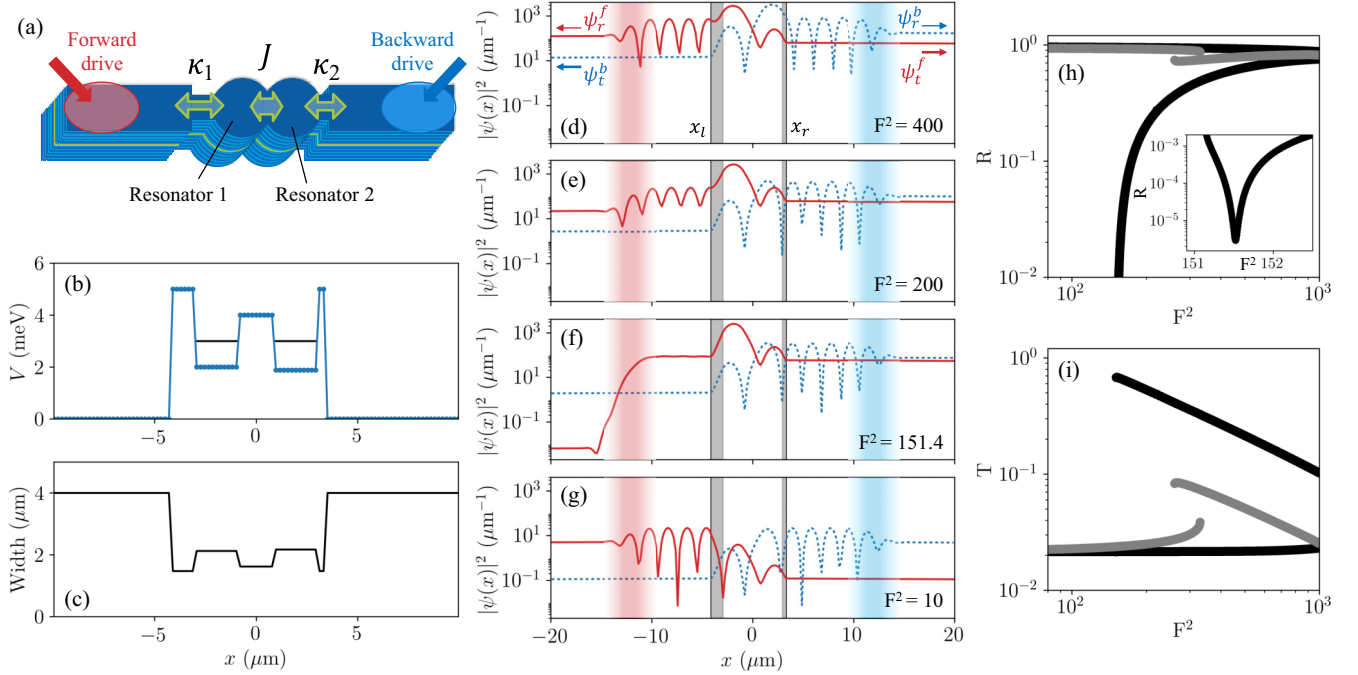
FIG. 6. (a) Sketch of the proposed implementation of coupled nonlinear cavities with asymmetric coupling to external ports based on etched polariton structures. (b) Potential $V(x)$ used in Eq. (15). Black lines indicate the energy $\hbar\omega_0$ of the confined modes in the wells. (c) Lateral width of the 2D structure realizing the potential energy landscape in (b). (d)–(g) Spatially resolved density $|\psi(x)|^2$ for $\omega = 3.49$ meV and a drive intensity indicated in the bottom right corner. Full red (dashed blue) line is for the forward (backward) configuration, with a drive on the left (right) of the wells. Shaded regions indicate the position of the drive in the forward and backward propagation direction, respectively. The positions of the external barriers are shown in gray, and their outer edge position is denoted $x_{l,r}$ (solid black lines). (h), (i) Reflectance and transmittance of the device, for $\omega = 3.49$ meV, in the forward configuration as a black line and in the backward configuration as a gray line. The inset in (h) is a zoom on the reflectance dip, around the critical driving power $F_c^2 = 151.4$.

this mapping by considering that the lateral confinement creates a local potential inversely proportional to w^2, w being the square of the structure width [49,50]:

$$V(x) = \hbar^2/2m[\pi/w(x)]^2. \qquad (14)$$

For strong lateral confinement, the different transverse modes of the waveguide are far apart in energy. Thus, we can safely consider only the lowest energy band with an effective polariton mass m.

The evolution of the polariton wave function $\psi(x, t)$ in a potential landscape $V(x)$ is governed by the following driven-dissipative 1D Gross-Pitaevskii equation [42,51]:

$$i\hbar\frac{\partial\psi(x,t)}{\partial t} = \left(-\frac{\hbar^2}{2m}\frac{\partial^2}{\partial x^2} + \hbar U|\psi(x)|^2 - i\frac{\hbar\gamma}{2}\right)\psi(x,t)$$
$$+ V(x)\psi(x,t) + i\mathcal{F}(x)e^{-i(\omega t - kx)}, \qquad (15)$$

where $\hbar U$ is the repulsive polariton-polariton interaction energy and γ is the decay rate. The last term in Eq. (15) corresponds to a monochromatic driving field of amplitude $\mathcal{F}$, frequency ω, and wave vector k. We compute the steady-state solutions of Eq. (15) with $m = 3 \times 10^{-5}m_e$ (m_e is the free-electron mass), $\hbar U = 0.3$ μeV μm, and $\hbar\gamma = 20$ μeV. These values are taken from recent experiments [36,52].

Next, we explain how we tailor the potential $V(x)$ in order to realize the nonreciprocal coupled-cavity design. We target a coupling between left and right confined modes $J = 100$ μeV and couplings to the waveguides $\kappa_1 = 60$ μeV and $\kappa_2 = 450$ μeV. According to Fig. 5, these values should yield both zero reflectance and good isolation at the optimal Δ [given by Eq. (13)].

Our approach to define $V(x)$ in relation to the zero-dimensional model is based on solving Eq. (15) for values of F where the interaction term $\hbar U|\psi(x)|^2$ is negligible and the response is linear to a very good approximation. We begin by considering a potential landscape with a single well [corresponding to either of the two wells in Fig. 6(b)]. For a well of length 2 μm, there is a single confined mode therein, with confinement energy $\omega_0 = 3.0$ meV. Next, we add a single potential barrier to tailor the coupling of the well to the waveguide. Leakage of polaritons from the well through the barrier broadens the confined mode linewidth. The coupling is extracted from this broadened linewidth. For a barrier height of 3 meV, $\kappa_1 = 60$ μeV is achieved with a barrier length 1.2 μm, and $\kappa_2 = 450$ μeV is achieved with a length 0.4 μm. Finally, to design the height of the barrier between the two cavities to the desired value of the coupling J, we consider coupled wells similar to those in Fig. 6(b) but with external barriers of effectively infinite thickness. The central barrier creates an effective coupling of amplitude J for polaritons between the wells. This leads to bonding and antibonding modes with energies $\omega_0 - J$ and $\omega_0 + J$, respectively. We find that a barrier of height 2 meV and length 1.9 μm is required to get the desired $J = 100$ μeV. We assume that J is not affected by the finite width of the barriers connecting the cavities to the 1D channels. The

potential $V(x)$ resulting from the above design is shown in Fig. 6(b), and the width of the corresponding 2D structure for an experimental implementation is shown in Fig. 6(c). Note that in Fig. 6(b) the reference for the potential ($V = 0$) corresponds to the confinement potential in the waveguides, of width 4 μm.

Forward and backward configurations are considered in order to determine the transmission and isolation properties of the device. The drive is either on the left of the double well and injects polaritons propagating toward the right (forward configuration), or the opposite (backward). These two situations are described in Eq. (15) with a drive term $\mathcal{F}_{f,b}(x) = Fe^{-(x-x_{f,b})^2/2\sigma^2}$, corresponding to a spot of Gaussian shape, centered on $x_{f,b} = \mp 12$ μm in the forward and backward configuration respectively. We choose a spot with 3 μm full width at half-maximum (FWHM) ($\sigma = 1.27$ μm). Additionally, the drive central wave vector $k_{f,b}$ is set to match the single polariton dispersion at energy $\hbar\omega$ to ensure efficient coupling with the modes in the external ports ($k_{f,b} = \pm\sqrt{2m\omega}/\hbar$).

We now investigate the performance of the proposed device in terms of isolation and suppression of reflectance. The steady-state density profiles in the wire, calculated for different drive intensities, are shown in Figs. 6(d)–6(g). The drive detuning $\Delta = \omega - \omega_0$ is fixed to $\Delta = 0.49$ meV for all cases. In the forward configuration (full red line), we define the transmitted field $\psi_t^f(x)$ as the field $\psi(x)$ on the right side of the right external barrier ($x > x_r = 3.35$ μm). In the backward configuration (dashed blue line), the transmitted field $\psi_t^b(x)$ is evaluated at the left of the left external barrier ($x < x_l = -4.15$ μm). The reflected field $\psi_r^{f,b}(x)$ is defined in a similar way. Two features in Figs. 6(d)–6(g) characterize the reflected field intensity in the forward configuration: (i) the polariton density $|\psi(x)|^2$ to the left of the pumping region ($x < -15$ μm), and (ii) the density modulation between the pumping region and the left external barrier ($-10 < x < -4.15$ μm), which results from the interference between the incident and scattered field. Starting from a high drive intensity $F^2 = 400$ [Fig. 6(d)], the difference of transmitted field intensity in the forward and backward configurations shows the nonreciprocal character of the device. However, the device is highly reflective, as indicated by the strong interference pattern for $-10 < x < x_l$. Decreasing the drive intensity to $F^2 = 200$ [Fig. 6(e)], we observe a reduced amplitude of the interference. Eventually, decreasing F^2 further, the interference has completely disappeared at $F^2 = 151.4$ [Fig. 6(f)]. This indicates a suppressed reflection, and correspondingly the polariton density is very low for $x < -15$ μm. Notice that nonreciprocal transmission is still observed at this critical drive $F_c^2 = 151.4$. This is no longer the case for a drive intensity $F^2 = 10$ [Fig. 6(g)], i.e., in the linear regime. In the absence of nonlinearities, the device has identical reflection and transmission properties whether in the forward or backward configuration.

To extract more quantitative information, we compute the transmittance and reflectance at a given F. From the calculated intensity profiles we extract the transmitted, reflected, and incident fields intensities $|\psi_{t,r,i}|^2$ at the external barriers position $x_{l,r}$. For example in the forward configuration, $\psi_r^f(x_l)$ is computed by extrapolating to x_l the slow exponen-
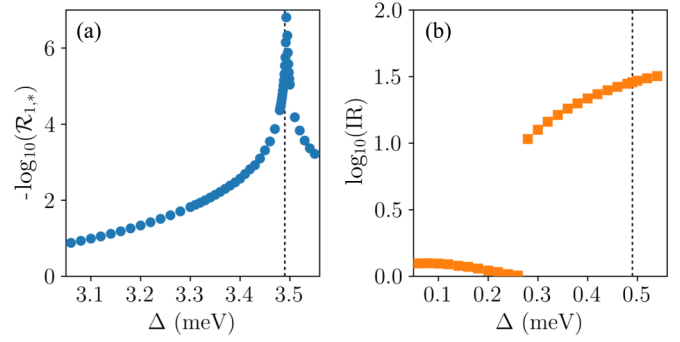

FIG. 7. (a) Minimum reflectance $\mathcal{R}_{1,*}$ observed for any value of F as a function of the detuning Δ. (b) Isolation ratio calculated at the value of F for which $\mathcal{R}_{1,*}$ was obtained. The dotted line indicates the detuning used in Figs. 6(d)–6(h).

tial decay at the left side. The incident field is deduced from the interference pattern in the region $-10 < x < x_l$ (a similar procedure is used for the backward configuration). Adapting the definition from the previous sections to the 1D model, the transmittance and reflectance are then given by $\mathcal{T}, \mathcal{R} = |\psi_{t,r}|^2/|\psi_i|^2$. Figures 6(h) and 6(i) show the calculated $\mathcal{R}, \mathcal{T}$ versus F^2 for $\Delta = 0.49$ meV in the forward (black) and backward (gray) configuration. We obtain the features predicted by the 0D model (Sec. II): a suppression of the reflectance down to less than 10^{-5} is observed when driving forward at a critical drive $F_c^2 = 151.4$. Moreover, at this critical drive intensity, the forward transmittance is 0.68 while backward transmittance is 0.024. This corresponds to an isolation ratio of 28 at F_c.

Similar to the discussion in the previous section, we extract the minimum value of $\mathcal{R}$ in the forward configuration when varying F for different values of the drive energy detuning Δ. We also compute the I at $\mathcal{R}_{1,*}$. The results, presented in Fig. 7, show that $\mathcal{R}_{1,*}$ becomes arbitrarily small around $\Delta = 0.494$ meV for finer steps in F and Δ. Values of $\mathcal{R}_{1,*}$ below 10^{-7} were not reached in the 1D calculations due to numerical rounding errors.

We note that with the values of $\kappa_{1,2}$ extracted from our design, the analytical expression (13) for the suppression of $\mathcal{R}$ in the 0D model gives $\Delta = 0.271$ meV. In the present case, we find $\mathcal{R}_{1,*} = 0$ for $\Delta = 0.494$ meV. This difference could be due to nonlinear spatial modifications of the modes in the double quantum wells. Indeed, we can see in Fig. 6(g), for instance, that the location of the density maxima within the two cavities depends on the excitation side. This distortion of the resonator modes, not captured by the 0D model, could modify the subtle interference effect responsible for $\mathcal{R}_{1,*} = 0$. Nevertheless, the results from the 1D simulations show that our simple 0D model captures all of the key features discussed previously: suppression of $\mathcal{R}$ and high isolation ratio. Experimentally, since the value of κ_2 is often not tunable after fabrication, the presence of two coupled cavities ensures that $\mathcal{R} = 0$ can be achieved by adjusting Δ.

IV. CONCLUSION

We have investigated the reflectance, transmittance, and nonreciprocity of single and coupled cavities with Kerr-type

nonlinearity under continuous driving and dissipation. We derived analytical expressions predicting the existence of unidirectional zero-reflectance states, and we verified these predictions with numerical calculations based on nonlinear coupled-mode theory and on the driven-dissipative Gross-Pitaevskii equation in one spatial dimension. We demonstrated how zero reflection and high nonreciprocity can be simultaneously obtained by tailoring the leakage rates of the cavities to their input-output ports. For a single cavity, zero reflection can only be achieved for one particular value of the input-output leakage rate difference. In contrast, for coupled cavities we have found that zero reflection can be achieved for any value of the leakage rates provided that one can tune the operation frequency. Finally, we have presented the design of an experimental structure on which our predictions could be tested. A limitation of our approach to simultaneously obtain zero reflection and nonreciprocity is that it is inherently limited in the operational power range, as expected due to the nonlinear origin of these effects. Nevertheless, we expect these results to assist in the design of nonlinear optical isolators, and other devices where light is intended to propagate one way only and with zero reflection at the input port.

APPENDIX A: COMPLEX FIELDS OF COUPLED CAVITIES

Here we explain how to solve Eqs. (9) and (10) to get the steady-state number of photons in the cavities n_j and the complex fields ψ_j ($j = 1, 2$). We start by rearranging equations (9) and (10) as follows:

$$\psi_1 = J^{-1}\left(-\Delta_2 - i\frac{\Gamma_2}{2} + Un_2\right)\psi_2, \quad (A1)$$

$$\psi_2 = \left[i\sqrt{\kappa_1}F + \left(-\Delta_1 - i\frac{\Gamma_1}{2} + Un_1\right)\psi_1\right]J^{-1}. \quad (A2)$$

To solve for $n_{1,2}$, we insert the expression for ψ_1 in Eq. (A1) into Eq. (A2), and then we multiply both sides with their complex conjugates. This leads to a polynomial equation (of order 9) in powers of n_2. Each root of that polynomial, subject to the physical condition $n_2 > 0$, corresponds to a steady state. Next, we can use the solutions for n_2 and Eq. (A1) to calculate n_1.

We now seek expressions for the complex field ψ_j, which is related to n_j via $\psi_j = \sqrt{n_j}e^{i\phi_j}$. Using this relation in Eqs. (A1) and (A2), we arrive (after some algebra) at the following expressions for the phase factors:

$$e^{i\phi_1} = \frac{\sqrt{n_2}e^{i\phi_2}}{\sqrt{n_1}J}\left(-\Delta_2 - i\frac{\Gamma_2}{2} + Un_2\right), \quad (A3)$$

$$e^{i\phi_2} = \frac{Ji\sqrt{\kappa_1}F}{\sqrt{n_2}\left[J^2 - \left(-\Delta_1 - i\frac{\Gamma_1}{1} + Un_1\right)\left(-\Delta_2 - i\frac{\Gamma_2}{2} + Un_2\right)\right]}, \quad (A4)$$

from which the complex fields ψ_j can be constructed once the n_j's are known.

APPENDIX B: ANALYTICAL EXPRESSION FOR ZERO REFLECTION IN COUPLED CAVITIES

In this section we derive an analytical expression guaranteeing the existence of a zero-reflection state in coupled cavities. We begin the derivation by inserting the expression for ψ_2 in Eq. (10) into the expression for ψ_1 in Eq. (9). After rearranging, we obtain

$$0 = \left(-\Delta + Un_1 - i\frac{\Gamma_1}{2}\right)\psi_1 - \frac{J^2\psi_1}{-\Delta + Un_2 - i\frac{\Gamma_2}{2}} + i\sqrt{\kappa_1}F. \quad (B1)$$

According to Eq. (12), $\mathcal{R} = 0$ implies $F = \sqrt{\kappa_1}\psi_1$. Hence, let us insert this expression for F into (B1), and separate the real and imaginary parts. The equation for the real parts reads

$$0 = -\Delta + Un_1 - \frac{J^2}{(-\Delta + Un_2)^2 + \frac{\Gamma_2^2}{4}}(-\Delta + Un_2). \quad (B2)$$

Meanwhile, the equation for the imaginary parts reads

$$0 = \tilde{\Gamma}_1 - \frac{J^2}{(-\Delta + Un_2)^2 + \frac{\Gamma_2^2}{4}}\Gamma_2, \quad (B3)$$

where we have defined $\tilde{\Gamma}_1 = \kappa_1 - \gamma$.

Let us now rewrite Eq. (10) to get the following relation between the number of photons in the cavities:

$$\frac{n_2}{n_1} = \frac{J^2}{(-\Delta + Un_2)^2 + \frac{\Gamma_2^2}{4}}. \quad (B4)$$

On the one hand, inserting Eq. (B4) into Eq. (B2) leads to

$$(-\Delta + Un_1)n_1 = (-\Delta + Un_2)n_2. \quad (B5)$$

On the other hand, combining Eqs. (B4) and (B3) yields

$$\frac{n_2}{n_1} = \frac{\tilde{\Gamma}_1}{\Gamma_2}. \quad (B6)$$

Using Eqs. (B5) and (B6), we can now solve for n_1 and n_2. We use Eq. (B6) to substitute n_1 in Eq. (B5) and get the following equation for n_2:

$$0 = \left(1 - \frac{\Gamma_2}{\tilde{\Gamma}_1}\right)\left[-\Delta + U\left(1 + \frac{\Gamma_2}{\tilde{\Gamma}_1}\right)n_2\right]. \quad (B7)$$

One solution for Eq. (B7) is $\Gamma_2 = \tilde{\Gamma}_1$, which is equivalent to $\kappa_1 = \kappa_2 + 2\gamma$. As discussed in the main text, this corresponds to the solution for $\mathcal{R} = 0$ of a single resonator with intrinsic loss 2γ, as given by Eq. (5). Note that in this

case, Eq. (B6) imposes $n_1 = n_2$, i.e., equal population is both resonators, confirming that they behave as a single one.

Coming back to Eq. (B7), for $\Gamma_2 \neq \tilde{\Gamma}_1$ we get the expression for n_2 corresponding to a second branch of solution,

$$n_2 = \frac{\Delta}{U} \frac{\tilde{\Gamma}_1}{\tilde{\Gamma}_1 + \Gamma_2}. \tag{B8}$$

Finally, we insert Eq. (B8) into Eq. (B3), and after a little bit of algebra we get

$$\Delta^2 = (\kappa_1 + \kappa_2)^2 \left(\frac{J^2}{(\kappa_1 - \gamma)(\kappa_2 + \gamma)} - \frac{1}{4} \right). \tag{B9}$$

Note that we can also determine the value of the drive amplitude F_c corresponding to the above solution. To this end, we recall that $\mathcal{R}_1 = 0$ imposes $F = \sqrt{\kappa_1}\psi_1$. F is a real number, so in this case ψ_1 is also real and we have $\psi_1 = \sqrt{n_1}$. We use Eqs. (B6) and (B8) to obtain the expression for n_1, and finally we get the following expression for F_c:

$$F_c^2 = \frac{\Delta}{U} \frac{\kappa_1(\kappa_2 + \gamma)}{\kappa_1 + \kappa_2}. \tag{B10}$$

Equation (B9) constraints the parameters Δ, J, and $\kappa_{1,2}$ such that $\mathcal{R}_1 = 0$. Equation (B10) gives the drive F_c at which $\mathcal{R}_1 = 0$ is achieved.

In particular, when $\gamma = 0$, Eq. (B10) is symmetric to the switching of input ports $1 \leftrightarrow 2$. Exciting from each side leads to $\mathcal{R} = 0$, $\mathcal{T} = 1$: in this particular situation, the device is perfectly reciprocal.

---

[1] R. Carminati, J. J. Sáenz, J.-J. Greffet, and M. Nieto-Vesperinas, Reciprocity, unitarity, and time-reversal symmetry of the *S* matrix of fields containing evanescent components, Phys. Rev. A **62**, 012712 (2000).

[2] D. Jalas, A. Petrov, M. Eich, W. Freude, S. Fan, Z. Yu, R. Baets, M. Popović, A. Melloni, J. D. Joannopoulos *et al.*, What is—and what is not—an optical isolator, Nat. Photon. **7**, 579 (2013).

[3] H. Ramezani, T. Kottos, R. El-Ganainy, and D. N. Christodoulides, Unidirectional nonlinear $\mathcal{PT}$-symmetric optical structures, Phys. Rev. A **82**, 043803 (2010).

[4] L. Fan, J. Wang, L. T. Varghese, H. Shen, B. Niu, Y. Xuan, A. M. Weiner, and M. Qi, An all-silicon passive optical diode, Science **335**, 447 (2012).

[5] H. Lira, Z. Yu, S. Fan, and M. Lipson, Electrically Driven Nonreciprocity Induced by Interband Photonic Transition on a Silicon Chip, Phys. Rev. Lett. **109**, 033901 (2012).

[6] T. Espinosa-Ortega, T. C. H. Liew, and I. A. Shelykh, Optical diode based on exciton-polaritons, Appl. Phys. Lett. **103**, 191110 (2013).

[7] L. Fan, L. T. Varghese, J. Wang, Y. Xuan, A. M. Weiner, and M. Qi, Silicon optical diode with 40 dB nonreciprocal transmission, Opt. Lett. **38**, 1259 (2013).

[8] S. Ghosh, S. Keyvaninia, W. Van Roy, T. Mizumoto, G. Roelkens, and R. Baets, Adhesively bonded Ce:YIG/SOI integrated optical circulator, Opt. Lett. **38**, 965 (2013).

[9] D. L. Sounas, C. Caloz, and A. Alù, Giant non-reciprocity at the subwavelength scale using angular momentum-biased metamaterials, Nat. Commun. **4**, 2407 (2013).

[10] L. D. Tzuang, K. Fang, P. Nussenzveig, S. Fan, and M. Lipson, Non-reciprocal phase shift induced by an effective magnetic flux for light, Nat. Photon. **8**, 701 (2014).

[11] L. Chang, X. Jiang, S. Hua, C. Yang, J. Wen, L. Jiang, G. Li, G. Wang, and M. Xiao, Parity-time symmetry and variable optical isolation in active-passive-coupled microresonators, Nat. Photon. **8**, 524 (2014).

[12] B. Peng, Ş. K. Özdemir, F. Lei, F. Monifi, M. Gianfreda, G. L. Long, S. Fan, F. Nori, C. M. Bender, and L. Yang, Parity-time-symmetric whispering-gallery microcavities, Nat. Phys. **10**, 394 (2014).

[13] N. A. Estep, D. L. Sounas, J. Soric, and A. Alù, Magnetic-free non-reciprocity and isolation based on parametrically modulated coupled-resonator loops, Nat. Phys. **10**, 923 (2014).

[14] Y. Yu, Y. Chen, H. Hu, W. Xue, K. Yvind, and J. Mork, Nonreciprocal transmission in a nonlinear photonic-crystal fano structure with broken symmetry, Laser Photon. Rev. **9**, 241 (2015).

[15] A. Metelmann and A. A. Clerk, Nonreciprocal Photon Transmission and Amplification Via Reservoir Engineering, Phys. Rev. X **5**, 021025 (2015).

[16] Z. Shen, Y.-L. Zhang, Y. Chen, C.-L. Zou, Y.-F. Xiao, X.-B. Zou, F.-W. Sun, G.-C. Guo, and C.-H. Dong, Experimental realization of optomechanically induced non-reciprocity, Nat. Photon. **10**, 657 (2016).

[17] F. Ruesink, M.-A. Miri, A. Alù, and E. Verhagen, Nonreciprocity and magnetic-free isolation based on optomechanical interactions, Nat. Commun. **7**, 13662 (2016).

[18] Y. Kominis, T. Bountis, and S. Flach, The asymmetric active coupler: Stable nonlinear supermodes and directed transport, Sci. Rep. **6**, 33699 (2016).

[19] D. L. Sounas and A. Alù, Time-Reversal Symmetry Bounds on the Electromagnetic Response of Asymmetric Structures, Phys. Rev. Lett. **118**, 154302 (2017).

[20] M. Lawrence, D. R. Barton, and J. A. Dionne, Nonreciprocal flat optics with silicon metasurfaces, Nano Lett. **18**, 1104 (2018).

[21] D. L. Sounas, J. Soric, and A. Alù, Broadband passive isolators based on coupled nonlinear resonances, Nat. Electron. **1**, 113 (2018).

[22] Z. Yu and S. Fan, Complete optical isolation created by indirect interband photonic transitions, Nat. Photon. **3**, 91 (2009).

[23] K. Fang, Z. Yu, and S. Fan, Photonic Aharonov-Bohm Effect Based on Dynamic Modulation, Phys. Rev. Lett. **108**, 153901 (2012).

[24] K. Fang, Z. Yu, and S. Fan, Realizing effective magnetic field for photons by controlling the phase of dynamic modulation, Nat. Photon. **6**, 782 (2012).

[25] D. L Sounas and A. Alù, Non-reciprocal photonics based on time modulation, Nat. Photon. **11**, 774 (2017).

[26] D. Ballarini, M. De Giorgi, E. Cancellieri, R. Houdré, E. Giacobino, R. Cingolani, A. Bramati, G. Gigli, and D. Sanvitto, All-optical polariton transistor, Nat. Commun. **4**, 1778 (2013).

[27] Y. Shi, Z. Yu, and S. Fan, Limitations of nonlinear optical isolators due to dynamic reciprocity, Nat. Photon. **9**, 388 (2015).

[28] S. A. Mann, D. L. Sounas, and A. Alù, Nonreciprocal cavities and the time-bandwidth limit, arXiv:1804.07420.

[29] P. D. Drummond and D. F. Walls, Quantum theory of optical bistability. I. Nonlinear polarisability model, J. Phys. A **13**, 725 (1980).

[30] D. F. Walls and G. J. Milburn, *Quantum Optics*, SpringerLink: Springer e-Books (Springer, Berlin, 2008).

[31] H. M. Gibbs, *Optical Bistability: Controlling Light with Light*, Quantum Electronics Series (Academic, Orlando, 1985).

[32] H. M. Gibbs, S. L. McCall, and T. N. C. Venkatesan, Differential Gain and Bistability Using a Sodium-Filled Fabry-Perot Interferometer, Phys. Rev. Lett. **36**, 1135 (1976).

[33] S. R. K. Rodriguez, W. Casteels, F. Storme, N. Carlon Zambon, I. Sagnes, L. Le Gratiet, E. Galopin, A. Lemaître, A. Amo, C. Ciuti, and J. Bloch, Probing a Dissipative Phase Transition Via Dynamical Optical Hysteresis, Phys. Rev. Lett. **118**, 247402 (2017).

[34] D. Sarchi, I. Carusotto, M. Wouters, and V. Savona, Coherent dynamics and parametric instabilities of microcavity polaritons in double-well systems, Phys. Rev. B **77**, 125324 (2008).

[35] C. Ouellet-Plamondon, G. Sallen, F. Morier-Genoud, D. Y. Oberli, M. T. Portella-Oberli, and B. Deveaud, Spatial multistability induced by cross interactions of confined polariton modes, Phys. Rev. B **93**, 085313 (2016).

[36] S. R. K. Rodriguez, A. Amo, I. Sagnes, L. Le Gratiet, E. Galopin, A. Lemaitre, and J. Bloch, Interaction-induced hopping phase in driven-dissipative coupled photonic microcavities, Nat. Commun. **7**, 11887 (2016).

[37] Strictly speaking, the lower bound on J given by Eq. (13) is $J^2 > (\kappa_1 - \gamma)\gamma/4$, which is satisfied when $J > \kappa_1, \gamma$.

[38] S. Rahimzadeh Kalaleh Rodriguez, A. Amo, I. Carusotto, I. Sagnes, L. Le Gratiet, E. Galopin, A. Lemaitre, and J. Bloch, Nonlinear polariton localization in strongly coupled driven-dissipative microcavities, ACS Photon. **5**, 95 (2018).

[39] T. Sato, S. Makino, T. Fujisawa, and K. Saitoh, Design of a reflection-suppressed all-optical diode based on asymmetric l-shaped nonlinear photonic crystal cavity, J. Opt. Soc. Am. B **33**, 54 (2016).

[40] T. Sato, T. Fujisawa, and K. Saitoh, Design of a high-forward-transmission all-optical diode based on cascaded side-coupled photonic crystal cavities, J. Opt. Soc. Am. B **34**, 2493 (2017).

[41] C. Weisbuch, M. Nishioka, A. Ishikawa, and Y. Arakawa, Observation of the Coupled Exciton-Photon Mode Splitting in a Semiconductor Quantum Microcavity, Phys. Rev. Lett. **69**, 3314 (1992).

[42] I. Carusotto and C. Ciuti, Quantum fluids of light, Rev. Mod. Phys. **85**, 299 (2013).

[43] M. Abbarchi, A. Amo, V. G. Sala, D. D. Solnyshkov, H. Flayac, L. Ferrier, I. Sagnes, E. Galopin, A. Lemaître, G. Malpuech, and J. Bloch, Macroscopic quantum self-trapping and Josephson oscillations of exciton polaritons, Nat. Phys. **9**, 275 (2013).

[44] A. Dreismann, P. Cristofolini, R. Balili, G. Christmann, F. Pinsker, N. G. Berloff, Z. Hatzopoulos, P. G. Savvidis, and J. J. Baumberg, Coupled counterrotating polariton condensates in optically defined annular potentials, Proc. Natl. Acad. Sci. (U.S.A.) **111**, 8770 (2014).

[45] S. Dufferwiel, F. Li, A. A. P. Trichet, L. Giriunas, P. M. Walker, I. Farrer, D. A. Ritchie, J. M. Smith, M. S. Skolnick, and D. N. Krizhanovskii, Tunable polaritonic molecules in an open microcavity system, Appl. Phys. Lett. **107**, 201106 (2015).

[46] D. Urbonas, T. Stöferle, F. Scafirimuto, U. Scherf, and R. F. Mahrt, Zero-dimensional organic exciton polaritons in tunable coupled gaussian defect microcavities at room temperature, ACS Photon. **3**, 1542 (2016).

[47] B. Zhang, S. Brodbeck, Z. Wang, M. Kamp, C. Schneider, S. Höfling, and H. Deng, Coupling polariton quantum boxes in sub-wavelength grating microcavities, Appl. Phys. Lett. **106**, 051104 (2015).

[48] A. F. Adiyatullin, M. D. Anderson, H. Flayac, M. T. Portella-Oberli, F. Jabeen, C. Ouellet-Plamondon, G. C. Sallen, and B. Deveaud, Periodic squeezing in a polariton josephson junction, Nat. Commun. **8**, 1329 (2017).

[49] G. Dasbach, M. Schwab, M. Bayer, D.N. Krizhanovskii, and A. Forchel, Tailoring the polariton dispersion by optical confinement: Access to a manifold of elastic polariton pair scattering channels, Phys. Rev. B **66**, 201201 (2002).

[50] H. S. Nguyen, D. Vishnevsky, C. Sturm, D. Tanese, D. Solnyshkov, E. Galopin, A. Lemaître, I. Sagnes, A. Amo, G. Malpuech, and J. Bloch, Realization of a Double-Barrier Resonant Tunneling Diode for Cavity Polaritons, Phys. Rev. Lett. **110**, 236601 (2013).

[51] D. Gerace and I. Carusotto, Analog Hawking radiation from an acoustic black hole in a flowing polariton superfluid, Phys. Rev. B **86**, 144505 (2012).

[52] V. Goblot, H. S. Nguyen, I. Carusotto, E. Galopin, A. Lemaître, I. Sagnes, A. Amo, and J. Bloch, Phase-Controlled Bistability of a Dark Soliton Train in a Polariton Fluid, Phys. Rev. Lett. **117**, 217401 (2016).